



Impact of Ni doping on $\text{La}_{0.7}\text{Sr}_{0.3}\text{Ni}_x\text{Mn}_{1-x}\text{O}_3$ perovskite manganite materials



P. Thamilmaran^{a,b}, M. Arunachalam^{a,b}, S. Sankararajan^c, K. Sakthipandi^{d,*}

^a Department of Physics, Sri SRNM College, Sattur 626203, Tamil Nadu, India

^b Research Scholars in Physics, Manonmaniam Sundaranar University, Tirunelveli 627012, Tamil Nadu, India

^c Department of Physics, Unnamalai Institute of Technology, Kovilpatti 628503, Tamil Nadu, India

^d Department of Physics, Sethu Institute of Technology, Kariapatti 626115, Tamil Nadu, India

ARTICLE INFO

Article history:

Received 15 September 2014

Received in revised form

25 July 2015

Accepted 7 August 2015

Available online 8 August 2015

Keywords:

Perovskite manganites

Ultrasonic measurements

Curie temperature

Super exchange interactions

ABSTRACT

On-line ultrasonic measurements on $\text{La}_{0.7}\text{Sr}_{0.3}\text{Mn}_{1-x}\text{Ni}_x\text{O}_3$ perovskite manganite material ($x=0.01, 0.02$ and 0.03) were performed on the samples synthesised by solid state reaction technique. The XRD studies on the samples confirm the crystalline nature with single phase rhombohedral structure having R3C space group. The average size of the particles determined using SEM images are 0.587, 0.412 and $0.356\ \mu\text{m}$ for $x=0.01, 0.02$ and 0.03 respectively. The temperature dependent ultrasonic velocities and attenuation measurements on the samples were used to reveal the ferromagnetic to paramagnetic phase transition temperature (Curie temperature) 374, 358 and 342 K for the values of $x=0.01, 0.02$ and 0.03 respectively. In addition, ultrasonic measurements confirm that the increase in Ni doping concentration in $\text{La}_{0.7}\text{Sr}_{0.3}\text{Mn}_{1-x}\text{Ni}_x\text{O}_3$ perovskites leads to a decrease in Curie temperature. The change in $\text{Mn}^{3+}/\text{Mn}^{4+}$ ratio with the phase transition temperature was explained on the basis of variation in amplitude of observed anomaly in ultrasonic measurements. The replacement of Mn^{4+} ion by Ni^{2+} ion leads to a change in the structural parameters and in the concentration of Mn^{3+} and Mn^{4+} ions.

© 2015 Elsevier B.V. All rights reserved.

1. Introduction

Recently the manganite materials with the composition $\text{R}_{1-x}\text{A}_x\text{MnO}_3$ (R – rare earth elements like La, Nd, Pr, Sm and A – divalent alkaline elements like Ca, Ba, Sr) have been with considerable interest due to the special properties like colossal magneto resistance (CMR), metal–insulator (MI) transition, charge ordering (CO), paramagnetic (PM) to ferromagnetic (FM) phase transition, magneto caloric effect, magneto capacitance effect [1–4]. Recent studies on ABO_3 perovskite materials reveal significant results through the substitution of rare earth ions or alkaline earth ions at A site [5–7]. These results lead to a gradual change from anti-ferromagnetic (AFM) phase to FM metallic phase. This property shows significant magnetic, transport and electronic properties across the composition and temperature range [1,2,5]. The substitution of the above nature helps to keep $\text{Mn}^{3+}/\text{Mn}^{4+}$ ratio and the double exchange (DE) interactions. The DE interaction is the exchange of simultaneous transfer of electrons from Mn^{3+} to the oxygen and from the oxygen to the neighbouring Mn^{4+} ions. However, the substitution of the dopant leads to the distorted

lattice structure which destroys the uniformity of distance in Mn–O plane, the angle between $\text{Mn}^{3+}\text{--O--Mn}^{4+}$ and the original magnetic exchange interaction [8]. The ratio of $\text{Mn}^{3+}/\text{Mn}^{4+}$ and the exchange coupling will come to exist in the Mn–O plane. It is found that the metal-semiconducting transition and the FM coupling are very sensitive to these changes. Thus, it leads to wide range of applications like frequency switching devices, magnetic storage devices, magnetic refrigeration, sensor technology, fuel cells etc. [8–10].

Undoped LaMnO_3 is an AFM insulator [11]. While doping with divalent elements like Sr^{2+} gives rise to rich magnetic and electronic transport phenomena like AFM insulating, ferromagnetic (FM) insulating, FM metallic and paramagnetic (PM) insulating properties [12]. Nowadays $\text{La}_{1-x}\text{Sr}_x\text{MnO}_3$ perovskites have received a wide acceptance in view of their CMR effect in its FM phase. The doping of Sr in the place of La leads to a change from AFM insulating ground state to FM metallic state because of the increase in the number of holes from Mn^{3+} to Mn^{4+} [13]. The observed CMR effect near the transition temperature T_C is due to the mixed valence state of Mn caused by Mn^{3+} (spin $s=2$) in the parent atom LaMnO_3 to Mn^{4+} (spin $s=3/2$) in the doped SrMnO_3 [14,15]. The doping of alkaline ions converts trivalent Mn^{3+} ($t_{2g}^3e_g^1$) into tetravalent Mn^{4+} ($t_{2g}^3e_g^0$) and so it introduces the e_g levels.

* Corresponding author. Fax: +91 4566 308000/6.

E-mail address: sakthipandi@gmail.com (K. Sakthipandi).

These holes in the e_g -2p band appear near the Fermi energy level due to the proximity between the e_g and O^{2-} 2p energy level. The electron (hole) on the e_g orbital can hop between spin aligned Mn^{3+} and Mn^{4+} ion via O^{2-} ions due to Hund's coupling rule. This DE interaction [14,16,17] is expected to give rise to the ferromagnetism and metallic behaviour in this mixed valent perovskites. Besides the DE interaction, lattice effect, Jahn–Teller (JT) distortion and charge ordering may also be helpful in understanding CMR effect [18]. The change in Mn^{3+} –O– Mn^{4+} ions which is responsible for DE interaction can be brought out by doping at the Mn site [19,20].

Recently more attention has been given to the replacement of Mn site by non-magnetic and magnetic ions to explore more information about the structural, magnetic and transport properties. The doping of Ni on $La_{0.7}Sr_{0.3}MnO_3$ magnetic materials reveals a change in the Mn^{3+} –O– Mn^{4+} bond and there by destroys the DE interaction leading to an increase in the resistivity [21]. In these systems, such complex phenomena arise due to the spin and orbital degrees of freedom associated with the e_g electrons [22]. To identify the valence and position of Ni dopants in perovskite manganite structure, Rubin Stein et al. [23] investigated the properties of Ni doped $La_{2/3}Ca_{1/3}MnO_3$, and found that the Ni ions are in the +2 valance states. Recently, Zhang et al. [24] have observed that Ni dopants in $La_{0.7}Sr_{0.3}Ni_xMn_{1-x}O_3$, which replace Mn ions in the manganite host lattice, are Ni^{2+} ions by X-ray photoelectron spectra, X-ray absorption fine structure, X-ray absorption near edged structure and Fourier transformed spectroscopy. Similar observations are also recorded in the manganite doped with Cr, Co, Cu and Fe [25–27]. Thus, the introduction of Ni^{2+} ions into Mn site of $La_{0.7}Sr_{0.3}MnO_3$ influences the magnetic properties directly [24].

The replacement of Mn by Ni in the samples destroys the ratio of Mn^{3+} – O^{2-} – Mn^{4+} bonds. Therefore, the double exchange is weakened and the ferromagnetism is suppressed with the reduction in the transition temperature T_C . Likewise, the competition is reinforced between FM and AFM exchange interactions. The magnetic interactions in the nickel doped $La_{0.7}Sr_{0.3}MnO_3$ samples are different from that of the undoped $La_{0.7}Sr_{0.3}MnO_3$. This is attributed to the increase in AFM interaction pairs such as Mn^{4+} – Mn^{4+} , Ni^{2+} – Mn^{4+} , Ni^{2+} – Mn^{3+} , Ni^{2+} – Ni^{2+} due to the increase in Mn^{4+} caused by the substitution of Ni^{2+} [24,28].

In the present study, the CMR material $La_{0.7}Sr_{0.3}MnO_3$ has been chosen as the parent material. The magnetic ion Ni of different concentration as $x=0.01$, 0.02 and 0.03 are substituted in the Mn site of the perovskite sample $La_{0.7}Sr_{0.3}MnO_3$. The measured ultrasonic parameters such as longitudinal velocity, shear velocity and attenuation are used to explore the structure/lattice, phase transition and then to correlate with perovskite magnetic properties. The measured ultrasonic parameters are influenced by many parameters like Young's modulus, Rigidity modulus, Bulk modulus, internal friction, thermal expansion etc. The on-line ultrasonic measurements are used to obtain the elastic constants, the structural and phase transitions and are also used to correlate the difference among the physical properties of AFM, FM and PM phase these perovskite manganites [29].

2. Experimental details

2.1. Preparation of samples

Poly crystalline $La_{0.7}Sr_{0.3}Ni_xMn_{1-x}O_3$ perovskite manganite materials with different compositions namely $x=0.01$, 0.02 and 0.03 were prepared employing solid state reaction technique [24]. Analytically pure grade La_2O_3 (99.99%, SigmaAldrich), $SrCO_3$ (99.99%, SigmaAldrich), $MnCO_3$ (99.9%, SigmaAldrich), and NiO

(99%, Hi Media), were used without any further purification. The above powders with stoichiometric quantity were mixed well, then ground and calcinated in air at 900 K for 2 h. The powders obtained were ground to get a homogeneous mixture. That mixture was calcinated at 900 K in air for 2 h. The powders were ground and pressed into pellets with a diameter of 13 mm and a thickness of 4 mm using a stainless steel dye. The percentage of error in the measurement of thickness is ± 0.01 . Then, the pellets were sintered at 1200 K for 12 h in air and were cooled into room temperature. These sintered pellets (hereafter called LSNMO1, LSNMO2 and LSNMO3 respectively for the composition $x=0.01$, 0.02 and 0.03) were used for further characterisation studies.

2.2. X-ray diffractometry

The X-ray diffraction (XRD) patterns of the prepared LSNMO samples were obtained using powder X-ray diffractometer (X'PertPro, Analytical, Netherlands) at a scan range of 10–80° with an increment of 0.02° using Cu K α as the radiation source. By knowing the values of angle of diffraction (2θ) and full width half-maximum, the Miller indices (hkl), were used to obtain the lattice parameters and relative atomic position of atoms of the perovskite samples. The crystalline size (D_{XRD}) of LSNMO1, LSNMO2 and LSNMO3 samples was determined by the full width at half-maximum ($\beta_{1/2}$), Miller indices (hkl) and angle of diffraction (2θ) of the XRD peaks using Scherrer's equation

$$D_{XRD} = \frac{0.94\lambda}{\beta_{1/2} \cos \theta} \quad (1)$$

where λ ($=1.5406$ Å) is the wavelength of the source used in x ray radiation.

2.3. Density measurement

The density of the LSNMO samples was measured employing Archimedes principle using CCl_4 as a buoyant. The weights of the samples in air and buoyant, W_a and W_b respectively, were measured using a digital balance (Sartorius, Germany). The density of the samples was obtained using the formula [30]

$$\rho = \frac{W_a}{W_a - W_b} \rho_b \quad (2)$$

where ρ_b is the density of the buoyant. The experiment was repeated for five times and then the average value was taken as the density of the sample. The percentage of error in the measurement of density is ± 0.05 .

2.4. SEM and EDX studies

A scanning electron microscope (SEM) integrated with the energy dispersive analysis of X-ray spectrometer (EDAX; JEOL, JED5300) was used to obtain the images of the LSMNO manganite samples to explore the microstructure, morphology and the composition of the perovskite samples. The spectrometer was operated at an accelerating voltage of 30 kV.

2.5. Ultrasonic velocity and attenuation measurement

The ultrasonic velocities (U_L and U_S) and attenuation (α_L and α_S) of the samples were measured employing through transmission technique using an experimental setup over a wide range of temperature. The schematic diagram of the ultrasonic measurement set-up is shown in Fig. 1. The transmission and reception of ultrasonic wave signals were made employing a high power ultrasonic pulsar receiver (5900 PR; Olympus NDT, USA) and a high

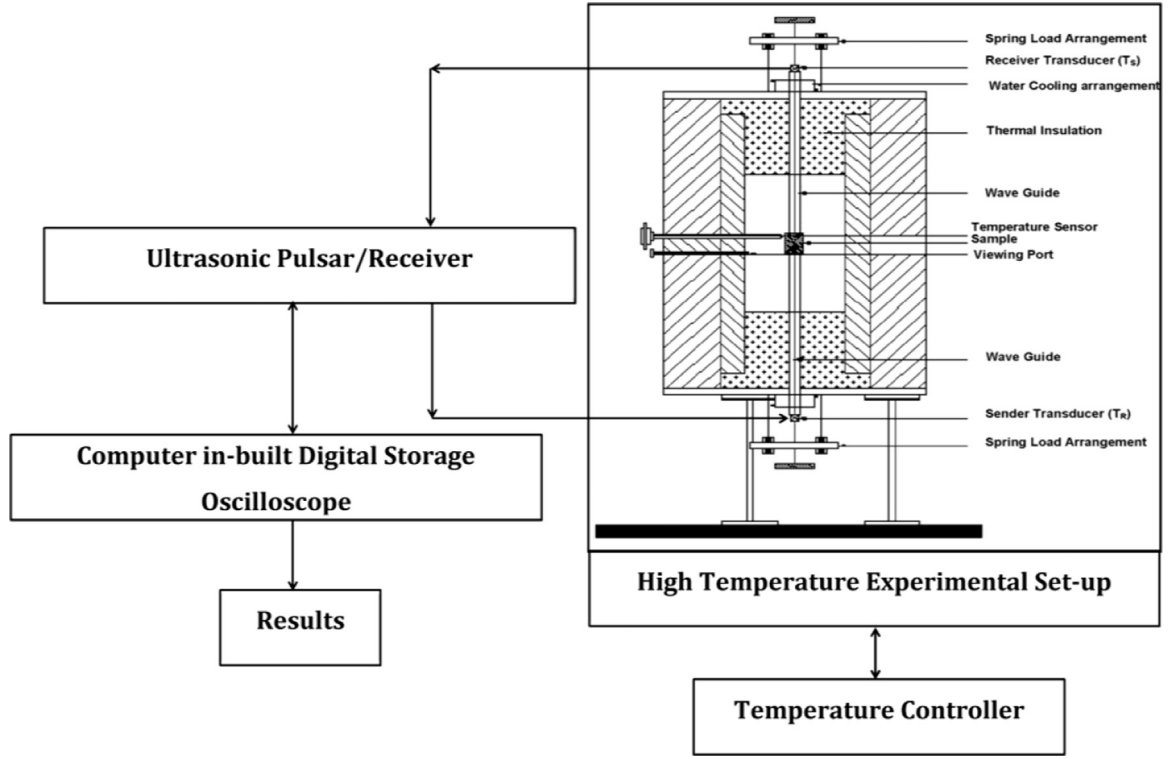


Fig. 1. The schematic diagram of the ultrasonic measurement set-up.

frequency (1 GHz) digital storage oscilloscope (Wave Runner104MXi; Lecroy, USA).

For the generation and the detection of the longitudinal and shear waves, a transducer with a fundamental frequency of 5 MHz was used. The required temperature in the chamber was controlled employing a programmable temperature controller (Eurotherm, 2604 USA). The temperature of the samples was gradually increased from 300 to 400 K at a uniform heating rate of 0.5 K min^{-1} . The accuracy in the measurement of temperature is $\pm 1 \text{ K}$. The ultrasonic velocities (U_L and U_S) of the perovskite samples were obtained using the equation [30]

$$U = \frac{d}{\Delta t} \quad (3)$$

where d is the thickness of the sample in micron resolution and transit time $\Delta t = (t_2 - t_1)$ is the time taken for the propagation of ultrasonic waves into the specimen which is in nano second resolution. It was obtained by measuring transit time t_1 (without the sample) just with the alumina rods and transit time t_2 (with the sample) by placing the sample between the two alumina rods (AD998, CoorsTek, USA). The overall accuracy in the measurement of velocity was $\pm 2 \text{ m s}^{-1}$. The transducer is coupled with the alumina rods and the sample using a suitable couplant (Honey) in order to get a steady back wall echo train which provides good impedance matching between the transducer, the sample and the alumina rods.

The amplitudes of the first and the second back wall echoes in the time domain trace were measured to obtain attenuation coefficient as follows [30,31]

$$\alpha(f) = \frac{1}{d} \left(\ln T + \ln \left(\frac{A_w(f)}{A_s(f)} \right) \right) \quad (4)$$

where $A_s(f)$ is the amplitude of the received signal with sample and $A_w(f)$ is the amplitude of the received signal without sample

$$T = \frac{4Z_w Z_s}{(Z_w + Z_s)^2} \quad (5)$$

where T is the transmission coefficient of the sample-wave guide interface, Z_w and Z_s are the acoustic impedance of the wave guide and the sample respectively. The percentage of error in the attenuation measurement is ± 2 .

Elastic constants of the samples were obtained from the measured ultrasonic velocities and density using the relations discussed in our earlier studies [30]

$$\text{Longitudinal modulus } L = U_L^2 \rho \quad (6)$$

$$\text{Shear modulus } G = U_S^2 \rho \quad (7)$$

$$\text{Bulk modulus } K = L - (4/3)G \quad (8)$$

$$\text{Young's modulus } E = (1 + \sigma)2G \quad (9)$$

$$\text{Poisson's ratio } \sigma = \frac{L - 2G}{2(L - G)} \quad (10)$$

The first differential function of ultrasonic velocity was obtained from the measured velocities as

$$\frac{\Delta U}{\Delta T} = \frac{U_2 - U_1}{T_2 - T_1} \quad (11)$$

3. Results and discussion

The XRD patterns of $\text{La}_{0.7}\text{Sr}_{0.3}\text{Ni}_x\text{Mn}_{1-x}\text{O}_3$ perovskite samples with different compositions of $x = 0.01, 0.02$ and 0.03 are shown in Fig. 2. The observed diffracted peaks of the samples at planes (0 1 2), (0 1 0), (1 0 4), (2 0 2), (0 0 6), (0 2 4), (0 1 8), (2 0 8) and (1 2 8) confirm the single phase rhombohedral structure with R3c space

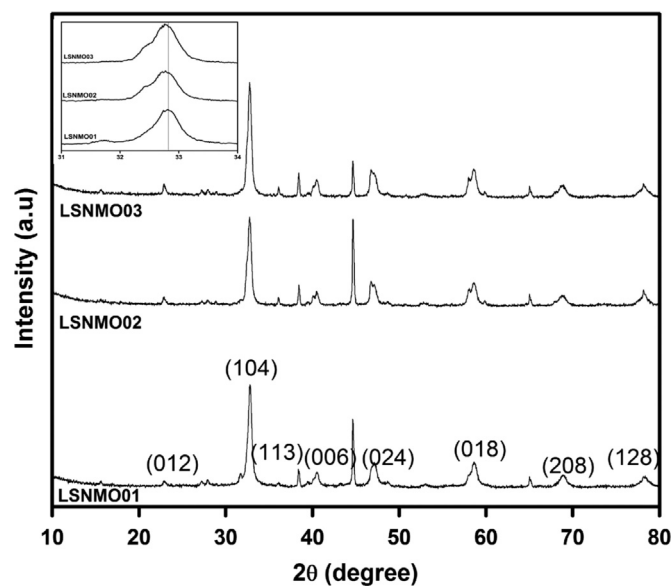


Fig. 2. X-ray diffraction patterns of LSNMO1, LSNMO2 and LSNMO3 perovskite manganite samples.

Table 1

Lattice parameters of the LSNMO1, LSNMO2 and LSNMO3 perovskite manganite samples.

Composition (x)	<i>a</i> (Å)	<i>c</i> (Å)	<i>c/a</i>	<i>V</i> (Å ³)
0.01	5.490	13.324	2.4269	347.7
0.02	5.489	13.359	2.4337	348.56
0.03	5.487	13.351	2.4332	348.10

group without the presence of any secondary phase [Joint Committee on Powder Diffraction Standards [JCPDS] file no. 51-0409 and 89-4461]. It is observed that as the composition of the doping material increases the diffraction peaks slightly shifted towards lower 2θ values (inset in Fig. 2). The crystalline size of the prepared samples obtained using Scherrer's equation of the XRD patterns are 0.1478, 0.1128 and 0.0940 μm for the samples LSNMO1, LSNMO2 and LSNMO3 respectively. Hence it is seen that an increase in Ni content leads to a decrease in crystalline size of the samples. The obtained lattice parameters *a* and *c* are given in Table 1. A decrease in lattice constant with an increase in the dopant concentration of Ni is observed, which agrees well with the results of Feng et al. [28]. This is ascribed due to an incorporation of Ni dopants to the manganite host lattice. It is to be noted that the substitution of Ni^{2+} ($r_{\text{ion}}=0.69$ Å) for Mn^{3+} ($r_{\text{ion}}=0.645$ Å) or Mn^{4+} ($r_{\text{ion}}=0.53$ Å) reduces the lattice parameters. Similar investigation was carried out on the role of Ni^{2+} ions in the structural, transport and magnetic properties of $\text{La}_{0.7}\text{Pb}_{0.3}\text{Mn}_{1-x}\text{Ni}_x\text{O}_3$. The above studies confirm that there is a slight decrease in the cell volume with the substitution of Ni^{2+} on the Mn site [32].

The morphology and composition of the samples are obtained from the recorded EDX/SEM images of the samples as shown in Figs. 3 and 4. It is observed that the EDX spectra of the perovskite samples are composed of La, Sr, Mn, O and Ni atoms. The atomic ratio of the elements obtained from the EDX spectra is shown in Fig. 3. It is clear from the EDX spectra that the atomic ratio of La, Sr, Mn, O and Ni atoms is in close agreement with that of the nominal composition of the starting atomic ratio of $\text{La}_{0.7}\text{Sr}_{0.3}\text{Ni}_x\text{Mn}_{1-x}\text{O}_3$ perovskite samples. The SEM micrographs of perovskite samples are shown in Fig. 4. The SEM micrographs of all the samples show a clear grain boundary. The average size of the particle of the samples is determined using the SEM images by finding the

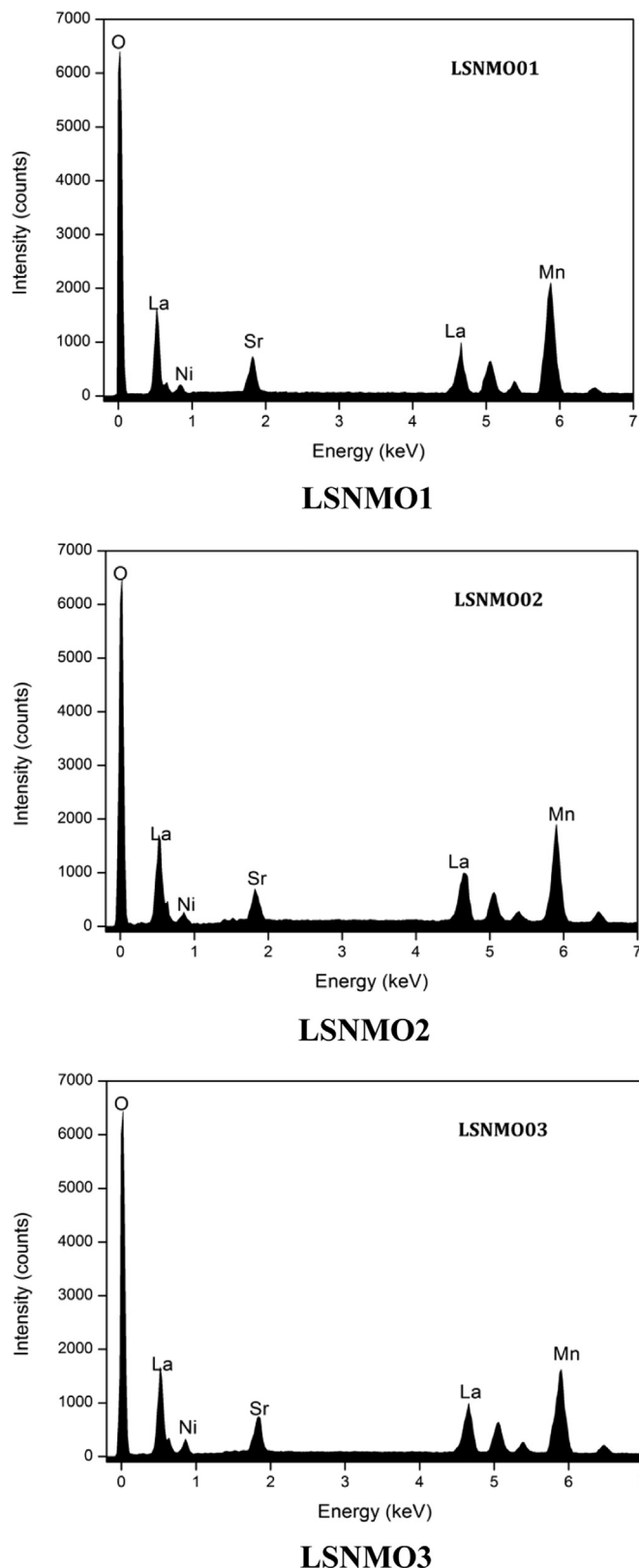
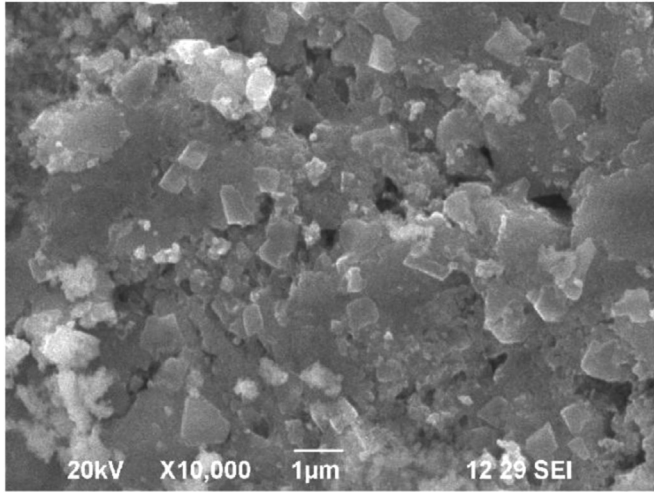
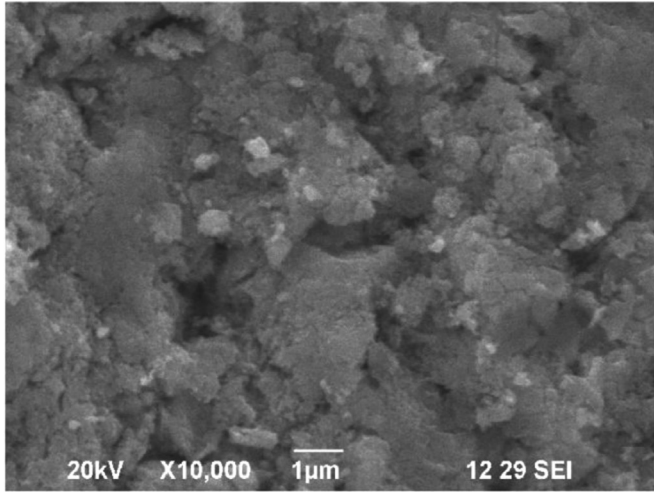


Fig. 3. EDAX patterns of LSNMO1, LSNMO2 and LSNMO3 perovskite manganite samples.

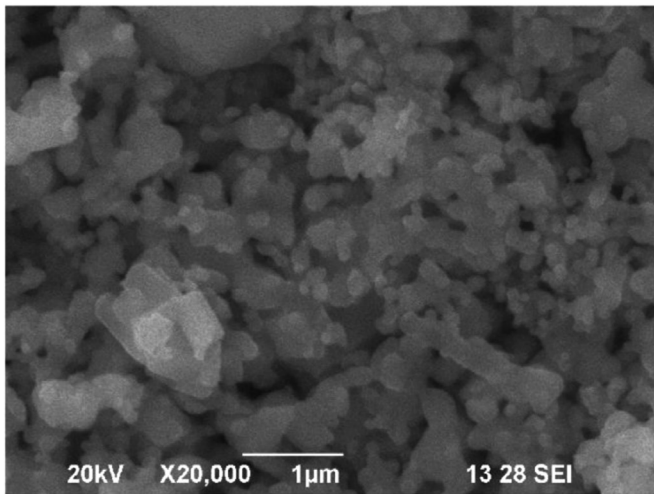
minimum and maximum dimension of the large number of particles. From the determined values it is observed that the average size of the particle of the sample decreases as the composition of Ni in the sample increases. It is evident from the fact that the



LSMNO1



LSMNO2



LSMNO3

Fig. 4. SEM images of LSMNO1, LSMNO2 and LSMNO3 perovskite manganite samples.

Table 2

Crystalline and particle size, density and the measured ultrasonic parameters at room temperature (300 K).

Parameter	LSMNO1	LSMNO2	LSMNO3
XRD – crystal size (μm)	0.1478	0.1128	0.094
SEM – particle size (μm)	0.481–0.673	0.327–0.541	0.212–0.475
Density (kg m^{-3})	6189	6338	6521
U_L (m s^{-1})	5877	5834	5775
U_S (m s^{-1})	2472	2446	2429
α_L (dB cm^{-1})	1.97	1.99	2.13
α_S (dB cm^{-1})	6.41	6.48	6.53
L (GPa)	213	215	217
G (GPa)	37	37	38
K (GPa)	163	165	166
E (GPa)	105	106	107

average size of particle of LSMNO1 is $0.587 \mu\text{m}$ while that of LSMNO2 and LSMNO3 are 0.412 and $0.356 \mu\text{m}$ respectively. The error in the measurement of the size of the particle is $\pm 0.04 \mu\text{m}$.

The measured density values of the prepared perovskite samples at room temperature are 6189 , 6338 and 6521 kg m^{-3} respectively for the samples LSMNO1, LSMNO2 and LSMNO3. It indicates that the value of density increases with the increase in the concentration of nickel content. It is due to the tight packing of the material, the doping level of Ni increases. Hence the increase in density occurs. The ultrasonic velocities and attenuation as a function of temperature were used to obtain information about various temperature dependent phase transition and its behaviour during the aging of the perovskite samples [30,33,34]. The measured ultrasonic velocities and attenuation along with the derived elastic moduli at room temperature are given in Table 2. From Table 2, it is observed that the ultrasonic velocity in both longitudinal and shear mode decreases while the density of the sample increases.

The temperature dependent longitudinal velocity (U_L), shear velocity (U_S), longitudinal attenuation (α_L) and shear attenuation (α_S) are shown in Figs. 5–8 respectively. The temperature dependent ultrasonic parameters show anomalous behaviour in the perovskite materials at T_C which is used to explore different phase transitions existing in the samples [30,33,34]. Generally, a monotonic decrease in velocity and an increase in attenuation with an increase in temperature are shown when there is no structural/phase transition in the perovskite manganite materials. However, an anomalous behaviour, a dip/peak in velocity/attenuation is

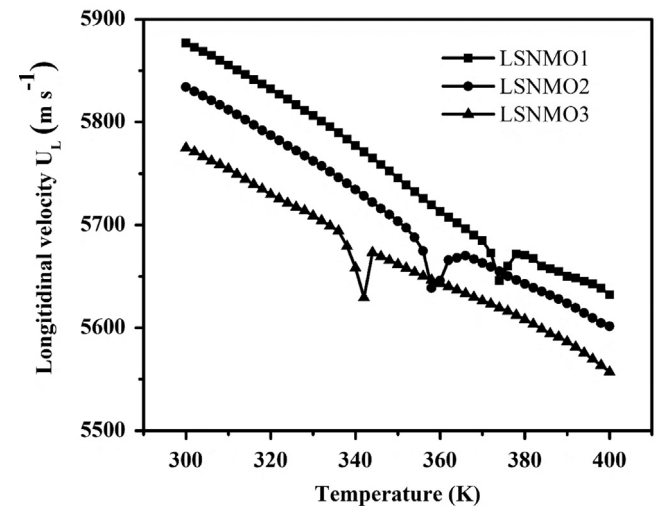


Fig. 5. Temperature dependence of longitudinal velocity of LSMNO1, LSMNO2 and LSMNO3 perovskite manganite samples.

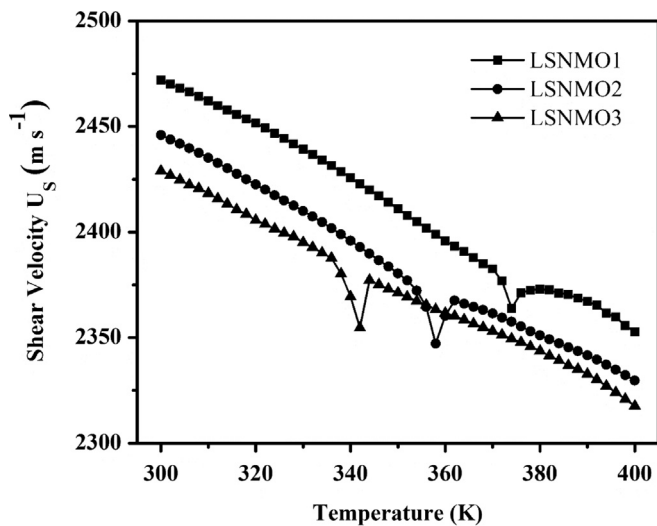


Fig. 6. Temperature dependence of shear velocity of LSNMO1, LSNMO2 and LSNMO3 perovskite manganite samples.

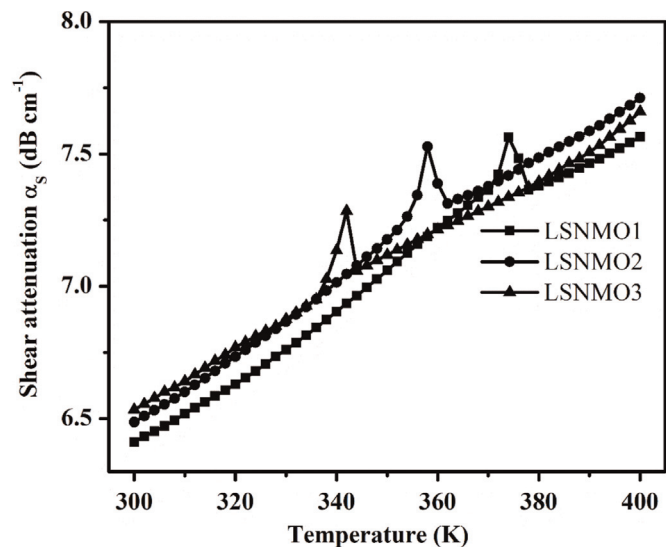


Fig. 8. Temperature dependence of shear attenuation of LSNMO1, LSNMO2 and LSNMO3 perovskite manganite samples.

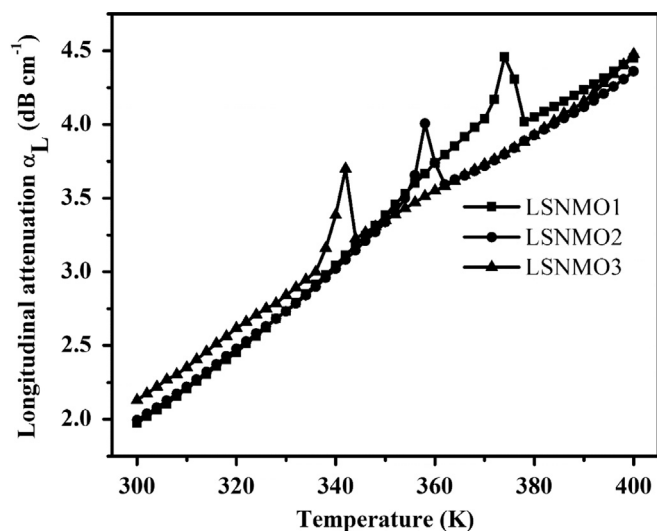


Fig. 7. Temperature dependence of longitudinal attenuation of LSNMO1, LSNMO2 and LSNMO3 perovskite manganite samples.

Table 3

Anomalous region of the LSNMO1, LSNMO2 and LSNMO3 perovskite manganite samples along with transition width in temperature and transition height in ultrasonic parameter.

Sample	LSNMO1	LSNMO2	LSNMO3
Starting temperature (K)	368	354	338
Anomalous temperature (K)	374	358	342
Ending temperature (K)	378	362	346
Transition width of the temperature (ΔT) K	10	8	8
Transition height of U_L (m s^{-1})	65	80	109
Transition height of U_S (m s^{-1})	28.5	46	55.5
Pronounced peak in first derivative ($\Delta U_L / \Delta T$) ($\text{m s}^{-1} \text{ K}^{-1}$)	22	30	36.5
Pronounced peak in first derivative ($\Delta U_S / \Delta T$) ($\text{m s}^{-1} \text{ K}^{-1}$)	10.25	15.39	18.58

observed at 354–362 K and 338–346 K and the Curie temperature for these samples are 358 and 342 K respectively. It is interesting to note that the temperature at which the velocity is minimum/attenuation is maximum is shifted towards lower temperature as the Ni content in the sample increases. There is a decrease in transition temperature with an increase in Ni content from $x=0.01$ to 0.03. The values of T_C and the magnetic entropy change (ΔS) in the samples are listed in Table 4. When the temperature increases the thermal phonons are generated in the lattice of the prepared samples. This leads to a monotonic decrease in the velocity and increase in attenuation. However, a strong interaction between the structure, the spin and the orbital exists at T_C . Thus, it causes a corresponding strain in the lattice.

The measured ultrasonic velocity and attenuation are directly linked with the lattice degrees of freedom which in turn causes the anomaly at the transition temperature. The observed decrease in T_C and ΔS in $\text{La}_{0.7}\text{Sr}_{0.3}\text{Ni}_x\text{Mn}_{1-x}\text{O}_3$ with an increase in Ni content may be attributed to the appearance of Ni^{2+} ions in the lattice. The additional contribution of super exchange interaction pairs of $\text{Mn}^{4+}-\text{Mn}^{4+}$, $\text{Ni}^{2+}-\text{Mn}^{4+}$, $\text{Ni}^{2+}-\text{Mn}^{3+}$, $\text{Ni}^{2+}-\text{Ni}^{2+}$ leads to reinforce the AFM phase [24]. When Ni^{2+} concentration increases, more Mn^{4+} ions are introduced into the lattice and hence, the concentration of Mn^{3+} ions is decreased. It is known that the electron–phonon interaction due to JT distortion leads to the localisation of charge carriers and weakens the importance of DE interaction and disfavours the metallicity and ferromagnetism [37].

obtained when a structural or phase transition occurs in the perovskite samples [34,35].

The observed dip in velocity and a peak in attenuation in LSNMO1, LSNMO2 and LSNMO3 samples are correlated with FM and AFM transition temperature. The temperature dependent ultrasonic parameters show both normal and anomalous behaviour. The starting, ending and maxima/minima anomalous temperatures of all the samples are observed and given in Table 3. Apart from the anomalous region, the ultrasonic parameters show a normal behaviour like that of solid material. A monotonic decrease in velocity and an increase in attenuation with the increase in temperature take place from 300 to 368 K (Zone I) and from 378 to 400 K (Zone III) in LSNMO1 sample. In the temperature region from 368 to 378 K, (Zone II) the sample shows an anomalous behaviour. The sudden decline in velocity starts from 368 K and reaches a minimum at 374 K, followed by a sharp increase in velocity up to 378 K. From the earlier phase transition studies [24,36], it is confirmed that the temperature at which the velocity is minimum in the anomalous region (Zone II) is the Curie temperature (T_C) of the perovskite sample. Similarly for the samples LSNMO2 and LSNMO3 anomalies in velocities and attenuation are

Table 4

Curie temperature T_C and Maximum magnetic entropy change ΔS_M for $\text{La}_{0.7}\text{Sr}_{0.3}\text{Mn}_{1-x}\text{Ni}_x\text{O}_3$ compared to $\text{La}_{0.7}\text{Sr}_{0.3}\text{MnO}_3$ based compounds.

Compound	T_C (K)	ΔS_M (J/kg K)	Reference
$\text{La}_{0.7}\text{Sr}_{0.3}\text{Mn}_{0.95}\text{Fe}_{0.05}\text{O}_3$	343	2.4	[27]
$\text{La}_{0.7}\text{Sr}_{0.3}\text{Mn}_{0.93}\text{Fe}_{0.07}\text{O}_3$	296	2.2	[27]
$\text{La}_{0.7}\text{Sr}_{0.3}\text{Mn}_{0.9}\text{Fe}_{0.1}\text{O}_3$	260	1.7	[27]
$\text{La}_{0.7}\text{Sr}_{0.3}\text{Mn}_{0.85}\text{Fe}_{0.15}\text{O}_3$	180	1.4	[27]
$\text{La}_{0.7}\text{Sr}_{0.3}\text{Mn}_{0.8}\text{Fe}_{0.2}\text{O}_3$	94	0.6	[27]
$\text{La}_{0.7}\text{Sr}_{0.3}\text{Mn}_{0.99}\text{Ni}_{0.01}\text{O}_3$	356	2.27	[24]
$\text{La}_{0.7}\text{Sr}_{0.3}\text{Mn}_{0.98}\text{Ni}_{0.02}\text{O}_3$	350	2.26	[24]
$\text{La}_{0.7}\text{Sr}_{0.3}\text{Mn}_{0.97}\text{Ni}_{0.03}\text{O}_3$	346.7	2.21	[24]
$\text{La}_{0.67}\text{Sr}_{0.33}\text{Mn}_{0.9}\text{Ni}_{0.1}\text{O}_3$	237	–	[21]
$\text{La}_{0.7}\text{Sr}_{0.3}\text{Mn}_{0.99}\text{Ni}_{0.01}\text{O}_3$	374	–	Present work
$\text{La}_{0.7}\text{Sr}_{0.3}\text{Mn}_{0.98}\text{Ni}_{0.02}\text{O}_3$	358	–	Present work
$\text{La}_{0.7}\text{Sr}_{0.3}\text{Mn}_{0.97}\text{Ni}_{0.03}\text{O}_3$	342	–	Present work
$\text{La}_{0.7}\text{Sr}_{0.3}\text{Mn}_{0.95}\text{Ni}_{0.05}\text{O}_3$	320	2.33	[43]
$\text{La}_{0.7}\text{Sr}_{0.3}\text{Mn}_{0.99}\text{Ni}_{0.01}\text{O}_3$	–	2.67	[43]
$\text{La}_{0.7}\text{Sr}_{0.3}\text{Mn}_{0.98}\text{Ni}_{0.02}\text{O}_3$	–	3.54	[43]
$\text{La}_{0.7}\text{Sr}_{0.3}\text{Mn}_{0.97}\text{Ni}_{0.03}\text{O}_3$	–	3.15	[43]
$\text{La}_{0.7}\text{Sr}_{0.3}\text{Mn}_{0.8}\text{Cr}_{0.2}\text{O}_3$	286	1.2	[45]
$\text{La}_{0.7}\text{Sr}_{0.3}\text{Mn}_{0.6}\text{Cr}_{0.4}\text{O}_3$	242	0.47	[45]
$\text{La}_{0.7}\text{Sr}_{0.3}\text{Mn}_{0.5}\text{Cr}_{0.5}\text{O}_3$	226	0.28	[45]
$\text{La}_{0.7}\text{Sr}_{0.3}\text{Mn}_{0.9}\text{Cu}_{0.1}\text{O}_3$	350	2.07	[44]
$\text{La}_{0.7}\text{Sr}_{0.3}\text{Mn}_{0.95}\text{Cu}_{0.05}\text{O}_3$	350	1.96	[44]
$\text{La}_{0.7}\text{Sr}_{0.3}\text{MnO}_3$	378	–	[30]
$\text{La}_{0.69}\text{Sr}_{0.31}\text{MnO}_3$	375	–	[30]
$\text{La}_{0.64}\text{Sr}_{0.36}\text{MnO}_3$	372	–	[30]

One can correlate the occurrence of decrease in velocity and increase in attenuation at the transition temperature to lattice softening [38]. Normally, a decrease in velocity and an increase in attenuation are observed due to the lattice softening while an increase in velocity and a decrease in attenuation are observed due to the lattice hardening [33,38]. The change in the strong link between the spin, the charge, the orbital and the lattice degrees of freedom and interaction at the transition temperature are responsible for the observed anomaly in ultrasonic velocities and attenuation [39,40]. The observed anomaly in ultrasonic parameters is not only correlated with the phase transition temperature T_C but also with the strong electron–lattice interactions through JT distortion of Mn^{3+}O_6 and spontaneous spin ordering below T_C .

The dip in anomaly region is ascribed to the magneto elastic coupling caused by the spin–phonon interaction in the samples. Moreover the coupling is due to the linear magnetostriction rather than the volume magnetostriction. This is confirmed by the fact that the anomaly occurs in both longitudinal and shear mode. In order to explain the observed anomaly in ultrasonic parameters, the transition width in temperature and the transition height in U_L and U_S of the observed anomaly were measured and given in Table 3. The transition height in longitudinal velocity (ΔU_L) of LSNMO1, LSNMO2 and LSNMO3 are 65, 80 and 109 m s^{-1} respectively. In the case of shear velocity (ΔU_S) the values are 28.5, 46 and 55.5 m s^{-1} for LSNMO1, LSNMO2 and LSNMO3 respectively. The increase in the transition height in velocities confirms the diminishing DE interaction of $\text{Mn}^{3+}-\text{Mn}^{4+}$ ions with an increase in Ni content [24].

Further, the increase in the transition height and the observed anomalies in both U_L and U_S indicate that the linear magnetostriction effect increases with the increase in Ni content [40]. As a result, the spin phonon interaction increases with the linear magnetostriction effect which in turn reduces the phase transition temperature T_C [40]. Thus, the observed anomaly in both the temperature dependent ultrasonic parameters supports the linear magnetostriction effect which is mainly due to spin–phonon interactions in LSNMO samples at T_C [17,35,40].

The vital observation made on the LSNMO samples is that the

area of anomalous region for ultrasonic longitudinal and shear velocity becomes narrower as the content of Ni increases in the sample. The area of the anomalous region has been calculated for Figs. 5 and 6 in Zone II. The area was calculated considering three points corresponding to the start, end and dip points of the anomalous region. The points are represented by the temperature and velocity (T, U) coordinates. The obtained values of the area are 421, 379 and 355 m s^{-1} K for longitudinal velocity and in the case of shear velocity 202.7, 196.8 and 189.6 m s^{-1} K in the LSNMO1, LSNMO2 and LSNMO3 respectively. The obtained decline in area is associated with the degree of disorder. Moreover, such narrowing of area in the anomalous region implies that addition of Ni changes the $\text{Mn}^{3+}/\text{Mn}^{4+}$ ratio. The interaction between Mn^{3+} and Mn^{4+} could exist in cluster surrounded by AFM host lattice and enhances the competition between FM and AFM interaction [24]. Thus, the ultrasonic measurements confirm that the magnetic entropy comes down with an increase in Ni content.

Further, the observed decrease in ultrasonic velocity and an increase in attenuation lead to an increase in acoustical activation energy E_p . The increase in E_p and thermally activated structural relaxation are responsible for the observed dip/peak in the ultrasonic velocities and attenuation at T_C which is due to the existence of a single relaxation process according to Arrhenius relation ($\tau = \tau_0 \exp(E_p/kT)$), as reported elsewhere [40]. The increase in acoustical energy E_p with an increase in Ni content in the perovskite samples is confirmed by the observed decrease in ultrasonic velocity and an increase in attenuation.

The observed dip in elastic modulus is used to ascertain the phase transition temperature of the perovskite samples [33,34]. From Fig. 9 it is seen that there is a decrease in the Young's modulus till it reaches T_C beyond which an increase in Young's modulus is observed. The observed increase and decrease in Young's modulus is correlated with lattice softening and hardening of perovskite manganite materials [33,38]. The observed dip in T_C is due to the occurrence of lattice hardening below T_C and lattice softening above T_C . The observed dip in the Young's modulus is an important factor for the CMR properties of perovskite materials.

When the Ni content in the samples increases, there is a large amount of substitution of Ni^{2+} into Mn^{3+} , hence the mobility of the charge carriers decreases since DE interaction is weakened. Such a decrease in carrier concentration leads to an increase in resistivity and a decrease in CMR [41,42]. Thus the increase in Ni

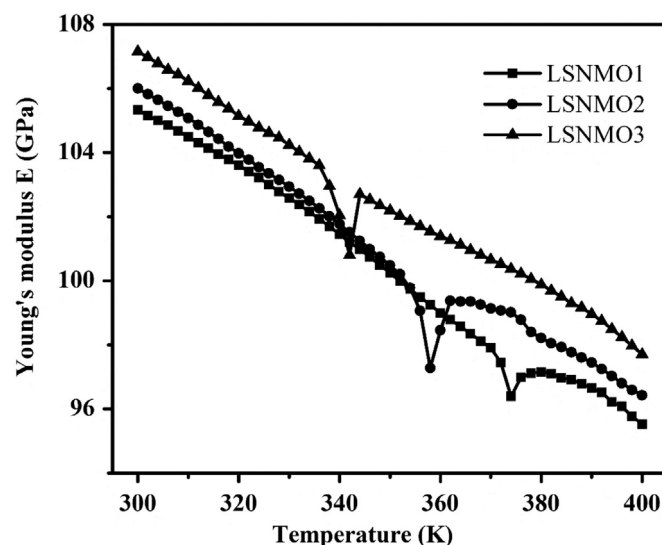


Fig. 9. Temperature dependence of Young's modulus of LSNMO1, LSNMO2 and LSNMO3 perovskite manganite samples.

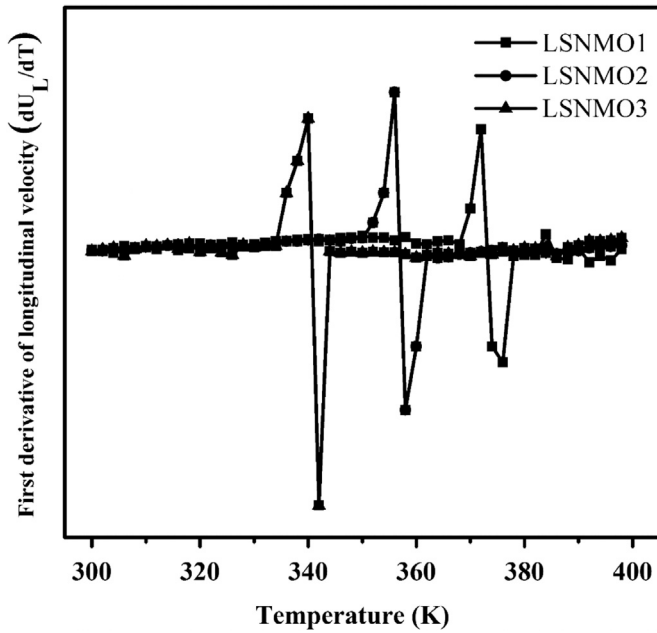


Fig. 10. Temperature dependence of first order differential of longitudinal velocity (dU_L/dT) of LSNMO1, LSNMO2 and LSNMO3 perovskite manganite samples.

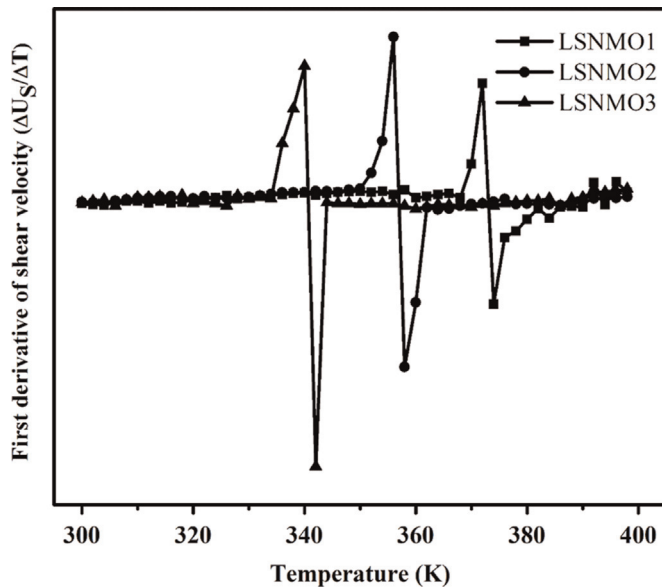


Fig. 11. Temperature dependence of first order differential of shear velocity (dU_S/dT) of LSNMO1, LSNMO2 and LSNMO3 perovskite manganite samples.

content leads to the competition between lattice degrees of freedom, orbital, charge and spin. Furthermore, it leads to a decrease in CMR. Hence the MI and FM transition become weak in LSNMO samples. The observed results show the direct evidence for coupling and interactions/competitions due to the effect of doping of Ni in perovskite samples.

To get the precise information on the temperature dependence of velocities, the first differential of both the velocities (U_L and U_S) as a function of temperature are plotted in Figs. 10 and 11 respectively. The values corresponding to the pronounced transition height around T_C are given in Table 3. They are 22, 30 and 36.5 $\text{m s}^{-1} \text{K}^{-1}$ for longitudinal velocity while they are 10.25, 15.39 and 18.58 $\text{m s}^{-1} \text{K}^{-1}$ for shear velocity in the samples LSNMO1, LSNMO2 and LSNMO3 respectively. The pronounced variation obtained in the ultrasonic variation in the first derivative

of the ultrasonic parameters is due to the larger fluctuations occurred in the lattice volume around the phase transition [35]. It is ascribed to the significant reduction in Jahn–Teller distortion of Mn^{3+}O_6 octahedral because of spin–lattice interaction below T_C . It is also observed that the pronounced variation in the observed minima in velocities at 374, 358 and 342 K respectively for LSNMO1, LSNMO2 and LSNMO3 samples which again confirms the phase transition temperature T_C .

The elastic modulus obtained from the ultrasonic measurement is used to explore the magnetic interaction and coupling in LSMNO perovskite samples. For single ion (linear) magnetostriction effect, there should be coupling to both transverse and longitudinal modes. As a result, a lattice softening at the transition temperature exists and this is evident from the observed longitudinal/shear velocities as well as attenuation studies. Due to the above properties such as diminishing DE interaction, reduction in CMR, decrease in T_C and ΔS , the Ni doped perovskite sample serves as a suitable material for the magnetic refrigeration application.

4. Conclusion

In the present study, $\text{La}_{0.7}\text{Sr}_{0.3}\text{Ni}_x\text{Mn}_{1-x}\text{O}_3$ perovskite samples for different Ni concentration ($x=0.01, 0.02$ and 0.03) were prepared. The structural properties of the prepared manganites were investigated employing X-ray powder diffraction method. The result shows a rhombohedral structure with single phase and R3c space group. The in-situ ultrasonic measurements on the samples reveal a decrease in T_C with an increase in Ni content. The decrease in ultrasonic velocity and an increase in attenuation with an increase in Ni content reveal the increase in acoustical activation energy E_p . The observed anomaly at T_C in both temperature dependent longitudinal velocity and shear velocity supports the linear magnetostriction effect which is mainly due to spin–phonon interaction in the perovskite samples. The increase in the height of transition in velocity as well as the width of temperature with an increase in Ni content confirms that an AFM phase is stronger than FM phase which is due to super exchange interaction pairs. From the above features, it is concluded that these Ni doped samples are suitable working substance in magnetic refrigeration application at room temperature.

References

- [1] R. VonHelmolt, J. Wecker, B. Holzapfel, L. Schultz, K. Samwer, *Phys. Rev. Lett.* 71 (1993) 2331–2333.
- [2] R. Mahesh, R. Mahendran, A.K. RayChaudhuri, C.N.R. Rao, *J. Solid State Chem.* 114 (1995) 297.
- [3] H. Kong, C. Zhu, *Appl. Phys. Lett.* 88 (2006) 41920–41926.
- [4] G. Tang, Y. Yu, W. Chen, Y. Cao, *J. Alloy. Compd.* 461 (2008) 486–489.
- [5] R. VanHelmolt, L. Haupt, K. Barner, U. Sondermann, *Solid State Commun.* 82 (1992) 693–696.
- [6] J. Hejmanek, Z. Jirak, D. Sedmidubsky, A. Maignan, C.H. Simon, V. Caignaert, C. Martin, B. Raveare, *Phys. Rev. B* 54 (1996) 11947–11950.
- [7] J.M. de Teresa, J. Balsco, M.R. Ibarra, J. Garcia, C. Marquina, P. Alagabel, A. de Morol, *Solid State Commun.* 96 (1995) 627–630.
- [8] J.M.D. Corey, *Adv. Phys.* 48 (1999) 167.
- [9] A. Kulkarni, F.T. Ciacchi, S. Giddey, C. Munnings, S.P.S. Badwal, J.A. Kimpton, D. Fini, *Int. J. Hydrog. Energy* 37 (24) (2012) 19092–19102.
- [10] Yuanbing Mao, Hongjun Zhou, Stanislaus S. Wang, *Mater. Matters* 5 (2) (2010) 50–57.
- [11] E.O. Wolan, W.C. Koehler, *Phys. Rev.* 100 (1955) 545.
- [12] G.H. Jonker, J.H. van Santen, *Physica* 16 (1950) 337–349.
- [13] S. Shimada, K. Kodaria, T. Matsushita, *J. Mater. Sci.* 19 (1984) 1385–1390.
- [14] P.G. de Gennes, *Phys. Rev. B* 118 (1960) 141–154.
- [15] C.N.R. Rao, A. Arulraj, P.N. Santhosh, A.K. Cheetham, *Chem. Mater.* 10 (1998) 2714–2722.
- [16] C. Zener, *Phys. Rev.* 82 (1951) 403–405.
- [17] P.W. Anderson, H. Hasegawa, *Phys. Rev.* 100 (1955) 675–681.
- [18] A.J. Millis, *Nature* 392 (1998) 147–150.
- [19] E. Banks, N. Tashima, *J. Appl. Phys.* 41 (1970) 1186–1187.

- [20] G.H. Jonker, *Physica* 20 (1954) 1118–1122.
- [21] Xin Chen, Zhihong Wang, Jain Wang cai, Bagoenshen, Wenshan Zhan, Jing Song Chen, *J. Appl. Phys.* 86 (1999) 4534–4538.
- [22] W. Prellier, P. Le Colur., B. Mercy, *J. Phys.: Condens. Matter* 13 (2001) R915–R944.
- [23] M. Rubinstein, D.J. Gillespie, J.E. Synder, T.M. Tritt, *Phys. Rev. B* 56 (1998) 5412–5423.
- [24] Y.D. Zhang, T.L. Phan, T.S. Yang, S.C. Yu, *Curr. Appl. Phys.* 12 (2012) 803–807.
- [25] O. Toulemonde, F. Studer, A. Barnabe, *Eur. Phys. J. B* 4 (1998) 159–167.
- [26] I.O. TroyanChuk, N.V. Samsonenko, A. Nabiaiek, H. Szymczak, *J. Magn. Mater.* 168 (1997) 309–315.
- [27] K. Barik, C. Krishnamoorthi, R. Mahendiran, *J. Magn. Mater.* 323 (2011) 1015–1021.
- [28] J.W. Feng, C. Ye, L.P. Hwang, *Phys. Rev. B* 61 (2000) 12271–12276.
- [29] Q.J. Huang, Y. Cheng, X.J. Liu, X.D. Xu, S.Y. Zhang, *Ultrasonics* 44 (2006) e1223–e1227.
- [30] S. Sankarajan, K. Sakthipandi, P. Manivasakan, V. Rajendran, *Phase Transit.* 84 (2011) 657–672.
- [31] P. He, *Ultrason. Imaging* 20 (1998) 275–287.
- [32] S. Pal, E. Bose, B.K. Chaudhuri, H.D. Yang, S. Neeleswar, Y.Y. Chen, *J. Magn. Mater.* 293 (2005) 872.
- [33] S. Sankarajan, K. Sakthipandi, V. Rajendran, *Phase Transit.* 85 (2012) 427–443.
- [34] K. Sakthipandi, V. Rajendran, T. Jeyakumar, *Mater. Res. Bull.* 48 (2013) 1651–1659.
- [35] R.K. Zheng, C.F. Shu, J.Q. Xie, R.X. Huang, X.G. Li, *Mater. Chem. Phys.* 75 (2002) 121–124.
- [36] M. Arunachalam, P. Thamilmaran, S. Sankarajan, K. Sakthipandi, *Physica B: Condens. Matter* 456 (2015) 118–124.
- [37] A.O. Sboychakov, K.I. Kugel, A.L. Rakhmanov, *Phys. Rev. B* 74 (2006) 014401–014431.
- [38] L. Hueso, N.D. Mathur, *Nature* 427 (2004) 301–303.
- [39] S.G. Min, K.S. Kim, S.C. Yu, H.S. Suh, S.W. Lee, *IEEE Trans. Magn.* 41 (2005) 2760–2762.
- [40] G.E. El-Falasky, M.S. Gaafer, N.S. Abd, El Aal, *Curr. Appl. Phys.* 12 (2012) 589–596.
- [41] M. Eshraghi, H. Salamati, P. Kameli, *J. Alloy. Compd.* 437 (2007) 22–26.
- [42] Ji-Weng Feng, C. Ye, Lian-Ping Hwang, *Phys. Rev. B* 61 (2000) 12271–12766.
- [43] Md.A. Choudhury, S. Akhter, D.L. Minh, N.D. Tho, N. Chau, *J. Magn. Mater.* 272–276 (2004) 1295–1297.
- [44] N. Chau, P.Q. Niem, H.N. Nhat, N.H. Luorg, N.O. Tho, *Physica B* 327 (2003) 214.
- [45] N. Kallel, S. Kallel, A. Hagaza, M. Oumezzine, *Physica B* 404 (2009) 285–288.